



Contents lists available at ScienceDirect

## International Journal of Solids and Structures

journal homepage: [www.elsevier.com/locate/ijsolstr](http://www.elsevier.com/locate/ijsolstr)

# A bar and hinge model formulation for structural analysis of curved-crease origami

Steven R. Woodruff, Evgueni T. Filipov\*

Department of Civil and Environmental Engineering, University of Michigan, Ann Arbor, MI 48109, USA



## ARTICLE INFO

## Article history:

Received 16 November 2019  
 Received in revised form 10 June 2020  
 Accepted 13 August 2020  
 Available online 28 August 2020

## Keywords:

Curved-crease origami  
 Mechanics of origami structures  
 Bar and hinge modeling  
 Anisotropic structures

## ABSTRACT

In this paper, we present a method for simulating the structural properties of curved-crease origami through the use of a simplified numerical method called the bar and hinge model. We derive stiffness expressions for three deformation behaviors including stretching of the sheet, bending of the sheet, and folding along the creases. The stiffness expressions are based on system parameters that a user knows before analysis, such as the material properties of the sheet and the geometry of the flat fold pattern. We show that the model is capable of capturing folding behavior of curved-crease origami structures accurately by comparing deformed shapes to other theoretical and experimental approximations of the deformations. The model is used to study the structural behavior of a creased annulus sector and an origami fan. These studies demonstrate the versatile capability of the bar and hinge model for exploring the unique mechanical characteristics of curved-crease origami. The simulation codes for curved-crease origami are provided with this paper.

© 2020 Elsevier Ltd. All rights reserved.

## 1. Introduction

In their flat state, thin sheets offer little in terms of design freedom and usability to engineers. Inspired by origami artists, researchers have found ways to increase the utility of these sheets by folding them about prescribed creases. Examples of origami solving engineering problems include lightweight and stiff deployable structures (Filipov et al., 2015), medical stents that can fold to a small form and unfold at vital points in the body (Kuribayashi et al., 2006; Rodrigues et al., 2017), and compactable solar arrays which take up little room in a spacecraft during launch and unfold to capture sunlight for power while in orbit (Miura, 1985; Tang et al., 2014).

One set of origami-inspired designs, called curved-crease origami, are created by folding thin sheets about arbitrary curves. The resulting three-dimensional shapes offer a variety of favorable structural features including bistability (Guest and Pellegrino, 2006; Giomi and Mahadevan, 2012; Bende et al., 2015), storage of elastic strain energy in the bent sheets (Woodruff and Filipov, 2018), and tunable, global stiffness isotropy for corrugations (Woodruff and Filipov, 2020). In contrast to straight-crease origami, curved-crease systems offer additional design freedom insofar as the shape of the crease, and by extension, the shape of the

folded sheet, includes infinite permutations (see Fig. 1 for examples). Such a broad set of designs could address engineering problems as shown by Tachi et al. (2011), Kilian et al. (2008), Kilian et al. (2017), Mitani and Igarashi (2011), Nagy et al. (2015).

As curved-crease origami are folded, both kinematics and the mechanics of sheet bending must be considered to describe the final deformed shape (Demaine et al., 2011). Furthermore, understanding the structural capacity and anisotropic stiffness of curved-crease origami during and after folding requires exploring the mechanics of the sheets beyond bending. The mechanics of straight-crease fold patterns such as the Miura-ori are well understood (Yang et al., 2016; Gattas and You, 2014), but mechanics literature has not explored curved-crease origami in great detail.

Early work by Huffman (1976) sought to describe the geometric features of curved-crease origami with further development by Duncan and Duncan (1784). The mathematical relationship between crease geometry and the shape of the folded sheet requires knowing, a priori, unintuitive parameters such as the deformed shape of the crease and the exact fold angle along the crease length. These relationships are useful, but would not benefit a designer starting from a flat fold pattern. Additionally, existing mathematical expressions for curved-crease folding apply to origami with just one fold or a tessellation of similar folds. These expressions do not work for origami with more than one fold, in general. Another method involves modeling the curved surfaces of folded sheets with Euler's elastica and reflecting the surface

\* Corresponding author.

E-mail address: [filipov@umich.edu](mailto:filipov@umich.edu) (E.T. Filipov).

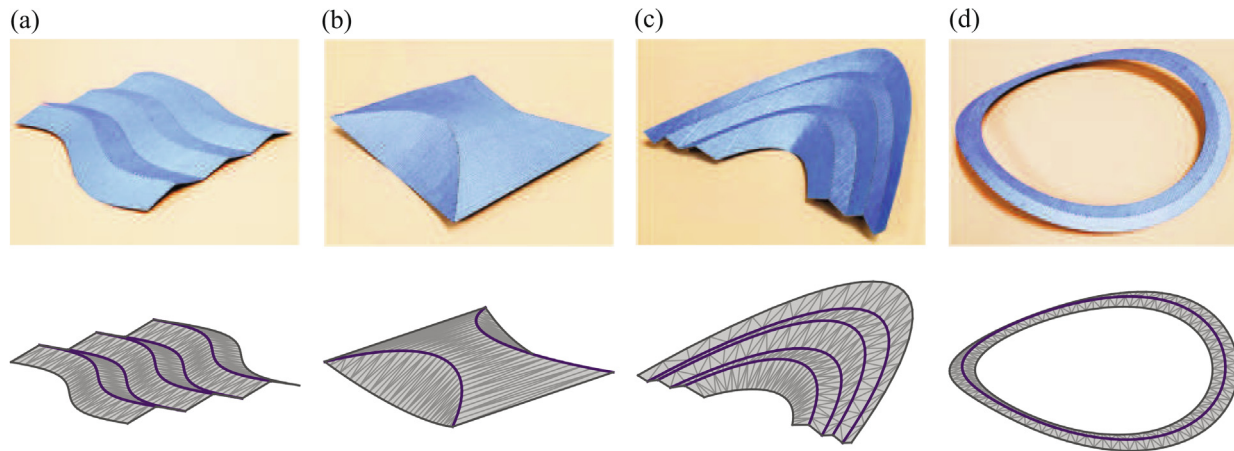


**Fig. 1.** The top row shows four photographs of paper, curved-crease origami constructed using a laser cutter and hand folding with the corresponding bar and hinge representations on the bottom row including (a) a sine wave tessellation, (b) a square with two parabolic curves, (c) a canopy made from parabolic curves, and (d) an annulus creased about mid-radius. These models are available in the [Supplementary code](#).

about mirror planes (Lee et al., 2018). However, this method does not necessarily allow for minimal energy states like flattening near free edges. While theoretical models like these are computationally efficient and elegant in their formulations, applications are limited. Many of the existing methods used to describe curved-crease systems rely on the assumption that folding and bending are the only deformation modes. However, there is evidence that stretching and shearing of the sheet in-plane, which are higher energy deformation states, also play an important role in the behavior of curved-crease structures (Dias et al., 2012). Thus, methods that can fold curved-crease origami and model the mechanics of origami after folding should also capture the non-negligible in-plane behaviors.

Finite elements have been used to model curved-crease origami starting from flat or pre-folded sheets (Vergauwen et al., 2017; Nagy et al., 2015; Woodruff and Filipov, 2018). These models allow for simulation of in-plane deformations and allow for a wider range of boundary conditions. However, finite elements can be cumbersome, with no guarantee that the formulations will be accurate, quick to implement, or that the model will converge, especially for systems with large curvatures or many folds.

In an effort to bridge the gap between limited theoretical methods and cumbersome finite element models, we offer a method for modeling curved-crease origami deployables that can capture the structural properties of a variety of curved-creased sheets with relative ease and accuracy. We improve an existing method for capturing the mechanics of straight-crease origami, called the bar and hinge model (Schenk et al., 2011; Filipov et al., 2017; Liu and Paulino, 2017; Gillman et al., 2018). We extend the capabilities of the model to describe the folding and post-folding structural behavior of curved-crease origami structures. We find that the model is applicable to curved-crease systems of arbitrary crease number and complexity for various sheet dimensions, elastic material properties, and structural boundary conditions. With this reformulation of the bar and hinge model, we can capture the folding, stiffness, elastic deformations, and nonlinear behavior of curved-crease origami systems.

This paper is organized as follows. In Section 2, we give background information on the bar and hinge method for modeling origami. In Section 3, we derive stiffness expressions from the material properties of the sheet and the geometry of the mesh for three main deformation modes: in-plane action, bending, and folding. In Section 4, we verify and explore these stiffness expressions using four methods: theoretical structural mechanics, differential geometry theory, experimental laser scanning, and folded shape simulations. Finally, in Section 5, we explore the anisotropy

of two curved-crease origami structures using the bar and hinge method with commentary on the strengths and limitations of the model.

## 2. Bar and hinge modeling of origami-inspired structures

The bar and hinge model is a simplified structural mechanics-based analytical method that captures the deformations and internal forces of thin sheets folded about straight creases (Schenk et al., 2011; Filipov et al., 2017; Liu and Paulino, 2017; Gillman et al., 2018). Bar and hinge models can capture the behavior of origami structures during folding as well as during loading after folding, a task that kinematic analysis cannot achieve. Relative to other mechanics models, such as finite elements, the bar and hinge method runs analyses quickly and is simple to implement with readily available parameters including a flat fold pattern, material properties, and prescribed fold angles. The ease and simplicity of bar and hinge models allow engineers to quickly understand and evaluate the structural properties of origami. The rapid analysis is especially useful when exploring proof-of-concept systems, running parametric studies, or performing optimization studies. State-of-the-art computer programs, such as MERLIN (Liu and Paulino, 2017) have been made available to the community, and are able to capture geometric and material non-linearity, essential to understanding the behavior of origami structures.

However, current bar and hinge models are designed for straight-crease or polyhedral origami systems. Additionally, these programs usually employ arbitrary stiffness values for elements when defining the properties of the sheet. Despite these limitations, there is potential for adapting and enhancing bar and hinge models to approximately capture the behavior of curved-crease origami.

The simplest bar and hinge model uses three types of elements that capture the structural properties of the system. Fig. 2(a–e) show how a sheet with a curved crease would be decomposed into these elements. The first element is a three-dimensional truss bar which only carries loads along its axis. These bars are connected at nodes which allow rotation, but not translation between the bars. When combined, the bars represent the in-plane stiffness of a thin sheet. The second element is a bending hinge, analogous to a spring coiled around a bar. This element serves the model by simulating the sheet bending stiffness. The third element is a folding hinge. Similar to the bending hinge, the folding hinge simulates the rotational stiffness of the material at the crease.

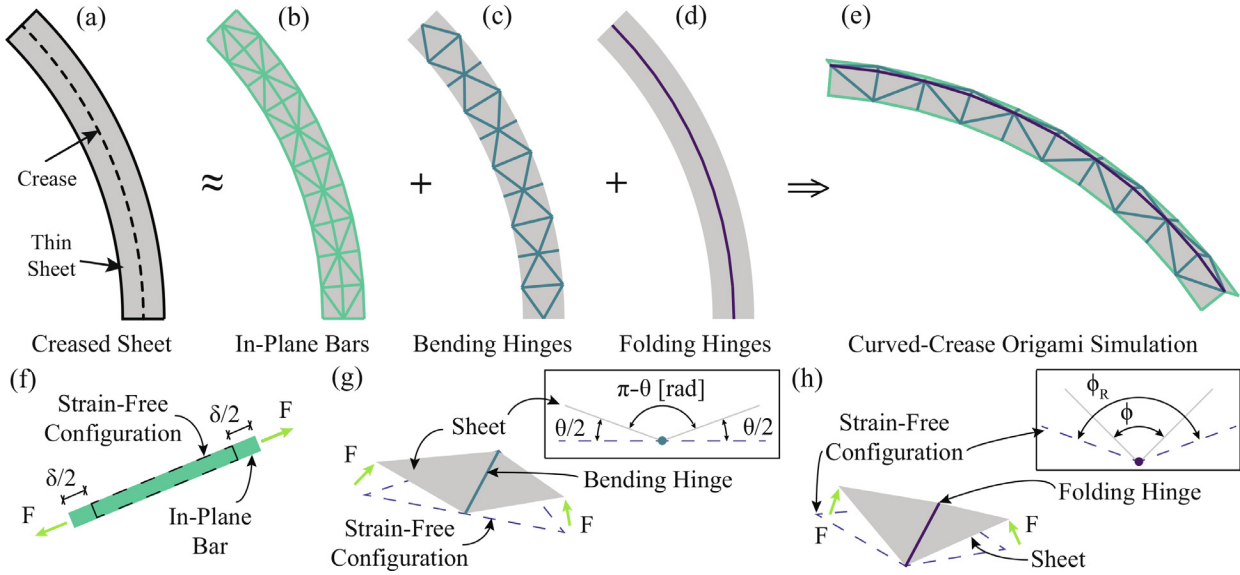


**Fig. 2.** The bar and hinge method works by representing (a) a creased, thin sheet using three elements: (b) bars to capture in-plane stretching and shearing, (c) bending hinges to capture sheet bending, and (d) folding hinges to capture crease folding. (e) The combination of all three elements simulates the deformed and folded shape of the sheet. Illustrations of element deformations due to a force,  $F$ , are shown for (f) bar extensions, (g) bending hinge rotations, and (h) folding hinge rotations. Inset images in (g) and (h) show a side-view with the hinge elements pointing out of the page.

The bar and hinge method works by calculating the total stiffness of the system using contributions from each element. The stiffness can be used to solve the equilibrium equation giving the forces and displacements of the system in response to arbitrary boundary conditions. The total strain energy in the system shows the relevant parameters of the analysis. That is,

$$U_{\text{total}} = \underbrace{\frac{1}{2} \sum_i k_s^i \delta_i^2}_{\text{bar energy}} + \underbrace{\frac{1}{2} \sum_j k_b^j \theta_j^2}_{\text{bending energy}} + \underbrace{\frac{1}{2} \sum_p k_f^p (\phi^p - \phi_R^p)^2}_{\text{folding energy}}. \quad (1)$$

Here,  $k_s^i$  is the stiffness of the  $i^{\text{th}}$  truss bar, and  $\delta_i$  is the corresponding extension of the bar (see Fig. 2(f)). The bending stiffness of the  $j^{\text{th}}$  hinge is  $k_b^j$ , and  $\theta_j$  is the rotation from the flat state (see Fig. 2(g)). Finally,  $k_f^p$  is the stiffness of the  $p^{\text{th}}$  folding hinge,  $\phi^p$  is the dihedral angle of the folding hinge, and  $\phi_R^p$  is the prescribed rest angle of the crease (see Fig. 2(h)). These values are either prescribed (for example, rest angles and stiffness coefficients) or calculated by converging to an equilibrium state (for example, bar extensions and hinge rotations).

By approximating curved creases with piece-wise linear bars, we can modify existing bar and hinge models for curved-crease origami. Additionally, we can relate the stiffness values of each element to the material properties and the geometry of the mesh such that the strain energy can be calculated based on the parameters explicitly defined by the designer.

### 3. Deriving element stiffness

In order to formulate the bar and hinge method for curved-crease origami without the use of arbitrary stiffness values, the stiffness of each of the three elements (in-plane bars, bending hinges, and folding hinges) should be calibrated to the mesh geometry and material properties of the sheet. In this section, we derive stiffness expressions for these elements starting from structural mechanics. We consider the three main deformation modes corresponding to the three model elements separately and verify the entire model in Section 4.

#### 3.1. In-plane bar stiffness

The bars used in the bar and hinge model capture deformations in the plane of the sheet. For curved-crease origami, the main deformation modes include tension in the sheet and shearing transverse to the length of the crease. Both of these deformations should be captured by the model such that the global deformation of the curved-crease system can be approximated (for instance, due to an applied load after folding). The material properties of the sheet, the dimensions, and the discretization of the mesh are considered in deriving the stiffness of the bars.

The stiffness of each bar is described by

$$k_s = \frac{EA_{\text{eff}}}{L}, \quad (2)$$

where  $E$  is the elastic modulus,  $A_{\text{eff}}$  is the effective cross-sectional area of the bar, and  $L$  is the length of the bar. The effective cross-sectional area of the bar must represent the cross-sectional area of the sheet in proportion to the geometry dimensions and the discretization. In order to determine an appropriate expression for  $A_{\text{eff}}$ , we calibrate the deflection of the bar and hinge model of a small section of the sheet to the deflection of a similar plane stress model of the same sheet for both shear and tension (see Fig. 3(a–c)). Our goal is to set the bar and hinge deflection,  $\Delta_{\text{BH}}$ , equal to the theoretical deflection value,  $\Delta_{\text{Th}}$  (that is, the deflection ratio,  $\Delta_{\text{BH}}/\Delta_{\text{Th}} = 1$ ).

Consider a triangular panel extracted from a sheet under uniform traction,  $F$ , as shown in Fig. 3(d). In this case, the cross-sectional area of the bar orthogonal to the traction (that is, the cross-sectional area of the top bar) must capture the cross-sectional area of the entire triangular panel. We can calculate an effective bar width by dividing the area of the triangle,  $A_T$ , by the length of the bar. Multiplying this value by the sheet thickness gives a lumped cross-sectional area of the sheet into the bar. The stiffness of such a bar is defined as,

$$k_s = \frac{EA_T t}{L^2}. \quad (3)$$

We quantify how the mesh is discretized using an aspect ratio,  $\alpha = H/W$ , where the panel height,  $H$ , is measured transverse to

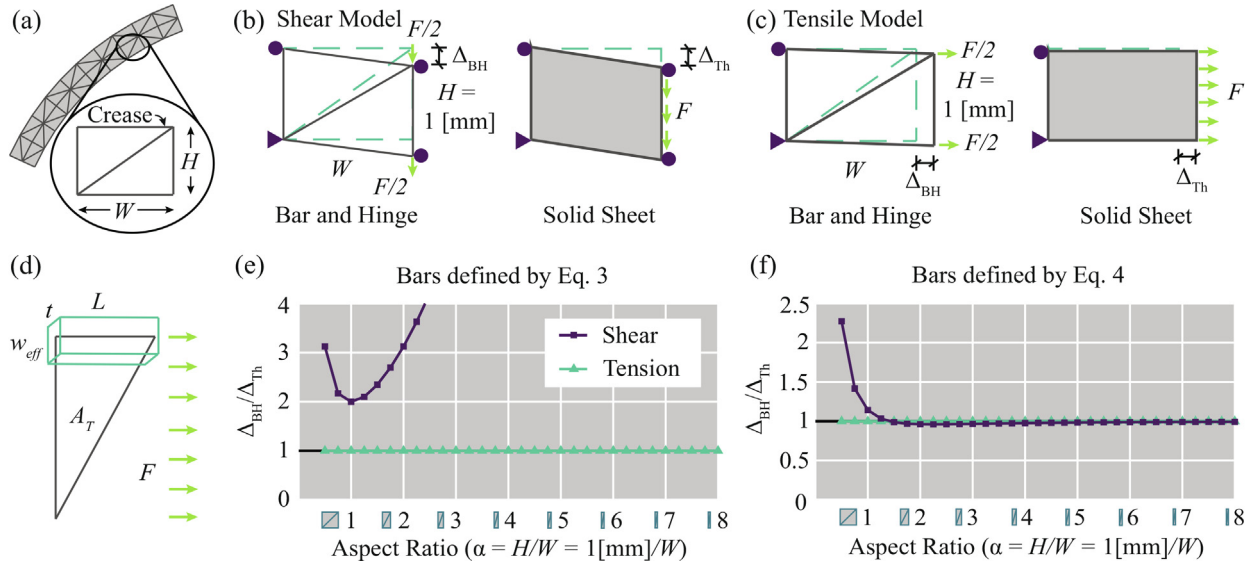


**Fig. 3.** The derivation for bar stiffness,  $k_s$ , starts by looking at (a) a one unit truss with width,  $W$ , parallel to the crease and height,  $H$ , perpendicular to the crease. The stiffness of the unit truss bars were calibrated for: (b) shearing transverse to the crease and (c) tension parallel to the crease. The bar and hinge deformations,  $\Delta_{BH}$ , were compared to those of a theoretical solid sheet,  $\Delta_{Th}$ . (d) The derivation for Eq. (3) came from spreading forces across a triangular panel into one bar. (e) The bar and hinge tensile and shear deformations versus the theoretical deformations when all bars are defined by Eq. (3). (f) The deformation comparison when the bars are defined by Eq. (4).

the crease and the panel width,  $W$ , is measured along the crease. In order to see how the bar and hinge model deflection changes with aspect ratio, we set  $H = 1$  [mm] and vary  $W$ .

Fig. 3(e) shows a comparison between the bar and hinge deflection with all bars defined by Eq. (3) and the deflection of the plane stress model. For tension, this stiffness definition matches theory for all aspect ratios. However, for shear, the bar and hinge model is too flexible, especially at large aspect ratios.

Noticing that the diagonal bar across the panel captures the shearing of the panel, we can increase the stiffness of just that element in proportion to the aspect ratio. Closer examination of Fig. 3 (e) shows that the shear deflection ratio diverges from theory at a quadratic rate for  $\alpha \geq 1$ . Indeed, a quadratic regression on the data shows that the deflection ratio varies with the aspect ratio as a function of the form  $\Delta_{BH}/\Delta_{Th}(\alpha) = \alpha^2/2 + 5/4$  with  $R^2 = 1.000$  for  $\alpha \in [1, 20]$ . This domain for the aspect ratio represents a reasonable boundary for discretization size since  $\alpha < 1$  will give an overly coarse approximation of the curved-crease geometry and  $\alpha > 20$  might not converge to a solution. In fact, we have observed that the condition number of the model increases at a nonlinear rate for  $\alpha > 12$ , which indicates more difficulty for convergence. As such, to better capture the shear behavior, we can increase the stiffness of the diagonal bar quadratically with the aspect ratio to reduce the flexibility in shear. Subsequently, the stiffness of the bars can be calculated as

$$k_s = \begin{cases} (\alpha^2/2 + 5/4) \frac{EA_T t}{L^2}, & \text{Diagonalbars} \\ \frac{EA_T t}{L^2}, & \text{Non - diagonalbars} \end{cases} \quad (4)$$

The deflection results are shown in Fig. 3(f) where we see that the tensile deflection always matches the theory and the shear deflection is within 1% of theory for  $\alpha > 1.5$ .

Another way we arrived at this solution was to assume that the bars had a stiffness defined as

$$k_s = \begin{cases} (a_2 \alpha^2 + a_1 \alpha + a_0) \frac{EA_T t}{L^2}, & \text{Diagonalbars} \\ \frac{EA_T t}{L^2}, & \text{Non - diagonalbars} \end{cases} \quad (5)$$

The coefficients  $a_2$ ,  $a_1$ , and  $a_0$  were then found by minimizing the deviation of the bar and hinge deflection from the theoretical deflection. Different values of the coefficients in the range  $a_2, a_1, a_0 \in [0, 10]$  were used against various aspect ratios  $\alpha \in [1, 20]$ . Using this metric, the optimal values of the coefficients which minimize the bar and hinge deflection errors are:  $a_2 = 1/2$ ,  $a_1 = 0$ , and  $a_0 = 5/4$ . Thus, both the optimization technique and quadratic regression method arrive at the same solution. Note that this solution applies to  $\alpha \in [1, 20]$  because this is a reasonable range for the mesh aspect ratio for curved-crease origami. It is possible to calibrate the shear response for low aspect ratios ( $\alpha < 1$ ), but because such a meshing is too coarse for curved-crease geometries, this task is out of the scope of this paper.

### 3.2. Bending hinge stiffness

When folding a flat sheet about a curved crease, sheet bending is the predominant deformation mode. The stiffness of the continuous sheet must be lumped into discrete bending hinges. In order to derive an expression for the bending stiffness, we use both the geometry of the mesh and the material properties of the sheet. We modify an elegant derivation by Dudte et al. (2016) to describe the bending stiffness.

Consider a flat sheet that has been folded about a curved crease. If we mesh this sheet with bar and hinge elements, we can look at one bending hinge at the interface of two panels with areas  $A_1$  and  $A_2$ , respectively (see Fig. 4(a)). The bending hinge has a length  $L$ . The two panels are rotated, relative to each other, by an angle  $\theta$ . The hinge elements must capture the bending of a sheet with thickness  $t$  and length  $s$ . The theoretical sheet length,  $s$ , is calculated later and is related to a representative bending region. If we assume that the region of the sheet that is taken from the curved surface is sufficiently narrow (that is, the mesh is fine), then we can assume that the sheet section represented by the bending hinge has constant curvature,  $\kappa$ .

The bending energy in the sheet should then be

$$U_{\text{sheet}} = \frac{1}{2} \int_0^s EI \kappa^2 ds = \frac{1}{2} EI \kappa^2 s, \quad (6)$$

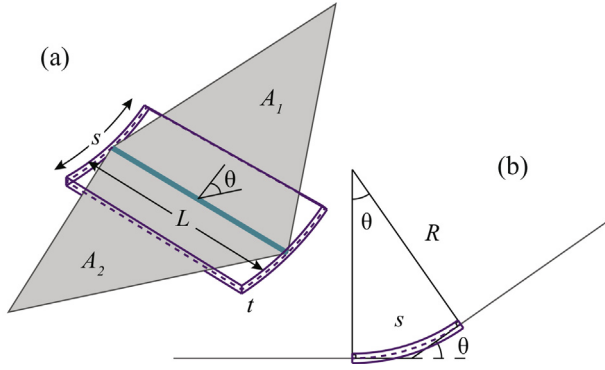


**Fig. 4.** The stiffness of one bending hinge connected to two triangular panels is derived by relating the strain energy in the hinge to that in an equivalent bent sheet of width,  $L$ , and length,  $s$ . (a) Top isometric view and (b) side view.

where  $E$  is the elastic modulus of the sheet and  $I$  is the second moment of area about the hinge calculated as  $I = Lt^3/12$ . Thus, the energy in the sheet section is

$$U_{\text{sheet}} = \frac{1}{2} \left[ \frac{Et^3}{12} L \kappa^2 \right] s. \quad (7)$$

The curvature of the sheet can be described by  $\kappa = 1/R$ . The length of the sheet is related to the rotation angle by  $s = R\theta$ . Rearranging gives  $R = s/\theta$ . Substituting this relationship into the curvature gives  $\kappa = \theta/s$ , and the strain energy in the sheet is

$$U_{\text{sheet}} = \frac{1}{2} \left[ \frac{Et^3}{12} \frac{L}{s} \right] \theta^2. \quad (8)$$

We want to constrain the area captured by the hinges such that the total area of the entire sheet is never exceeded. This area can be expressed as  $sL = (A_1 + A_2)/2$ . Rearranging gives  $s = (A_1 + A_2)/(2L)$ . We can substitute this expression into the sheet strain energy giving

$$U_{\text{sheet}} = \frac{1}{2} \left[ \frac{Et^3}{6} \frac{L^2}{A_1 + A_2} \right] \theta^2. \quad (9)$$

We set the energy in the bent sheet equal to the strain energy in the bending hinge,

$$U_{\text{hinge}} = \frac{1}{2} k_b \theta^2, \quad (10)$$

to solve for the stiffness coefficient for bending,  $k_b$ . This gives a bending stiffness of

$$k_b = \frac{Et^3}{6} \frac{L^2}{A_1 + A_2}. \quad (11)$$

We see that the bending stiffness is effectively the bending modulus of a sheet from mechanics,  $D_b = Et^3/(12[1 - \nu^2])$ , with  $\nu = 0$ , when multiplied by a non-dimensionalized parameter based on the mesh. As will be shown in Sections 4.1 and 4.2, this definition provides a converging solution for bending energy in the sheet.

### 3.3. Folding hinge stiffness

Deriving the rotational stiffness of a crease based on the system properties is not yet possible. Confounding parameters such as material properties, material damage at the crease, folding history, local crease design, and geometry of the sheet around the crease could all affect the stiffness. Existing literature on the subject is

mostly experimental (Lechenault et al., 2014; Beex and Peerlings, 2009; Huang et al., 2014; Mentrasti et al., 2013; Yasuda et al., 2013) and does not consider curved creases. Overall, there is no method to accurately predict the stiffness of a folding hinge directly from the material properties and mesh geometry.

A previous approach to modeling fold stiffness (Filipov et al., 2017; Lechenault et al., 2014) reduces the complexity of the crease into one equation. The model considers the bending modulus of the sheet,  $D_b$ , the length of the fold,  $L_f$ , and a length scale factor,  $L^*$ . The length scale factor is introduced for parameters not explicitly included in the stiffness expression. The fold stiffness is

$$k_f = \frac{L_f}{L^*} D_b = \frac{L_f}{L^*} \frac{Et^3}{12(1 - \nu^2)} \approx \frac{L_f}{L^*} \frac{Et^3}{12}, \quad (12)$$

where  $E$  is the elastic modulus of the sheet,  $t$  is the thickness, and  $\nu$  is the Poisson's ratio (for consistency with the bending derivation, we set  $\nu = 0$ ). The proper value of  $L^*$  for curved creases is problem-specific and can only be determined numerically by looking at the difference between the prescribed folding angle and the angle the model reaches after folding (see Section 4.4). For straight origami creases, typical values of  $L^*$  are in the range of 25 [mm] to 100 [mm] (Filipov et al., 2017). Despite the overall incompleteness of fold stiffness modeling, we use this approach to define the stiffness,  $k_f$ , of the folding hinges.

## 4. Verifying the element stiffness

To verify the accuracy of the element stiffness expressions, we employ four different methods to compare deformed shapes of the bar and hinge model to deformed shapes of other theoretical and experimental models. The deformed shape is a result of the element stiffness expressions and acts as a proxy for verifying the stiffness directly. The methods we conduct include (1) comparing the deformed shape of a strip of material under four types of loading to structural mechanics theories, (2) comparing the deformed shape of an annulus sector folded along its center to the shape of a cone section, (3) comparing the deformed shapes of complex curved-crease origami with multiple creases to point clouds from laser scanned physical paper models, and (4) exploring the relationship between fold stiffness, rest angle, and the actual fold angle simulated by the model. These verifications serve to show the accuracy of the results as well as the limitations of the bar and hinge method.

### 4.1. Thin strips under different load cases

Without considering folds, we can test to see how well the bending and the in-plane stiffness definitions capture the deformation of thin, long strips by comparing the strain energy in the bar and hinge model to structural mechanics solutions for the same problems. We model an isotropic, homogeneous strip using the bar and hinge method with linear-elastic material properties, and with various mesh sizes. In order to quantify the size of the mesh, we employ a metric called the aspect ratio,  $\alpha$ . Each triangular panel has an aspect ratio defined as the ratio of the side length perpendicular to the fold,  $H$ , to the side length roughly parallel to the fold,  $W$ . Because there is no fold in the strips, the aspect ratio is the ratio of the vertical side length to the horizontal side length when the strip is placed such that the long direction lies horizontally (see Fig. 5(b)). As such, a larger aspect ratio indicates a finer mesh discretization. The strip has a length of 10 [mm], a width of 1 [mm] (that is,  $H = 1$  [mm]), and a thickness of 0.1 [mm]. For clarity, we use familiar SI units; however, the units are arbitrary when consistent. The strip is restrained and loaded in four different ways (see Fig. 5(a–d)).

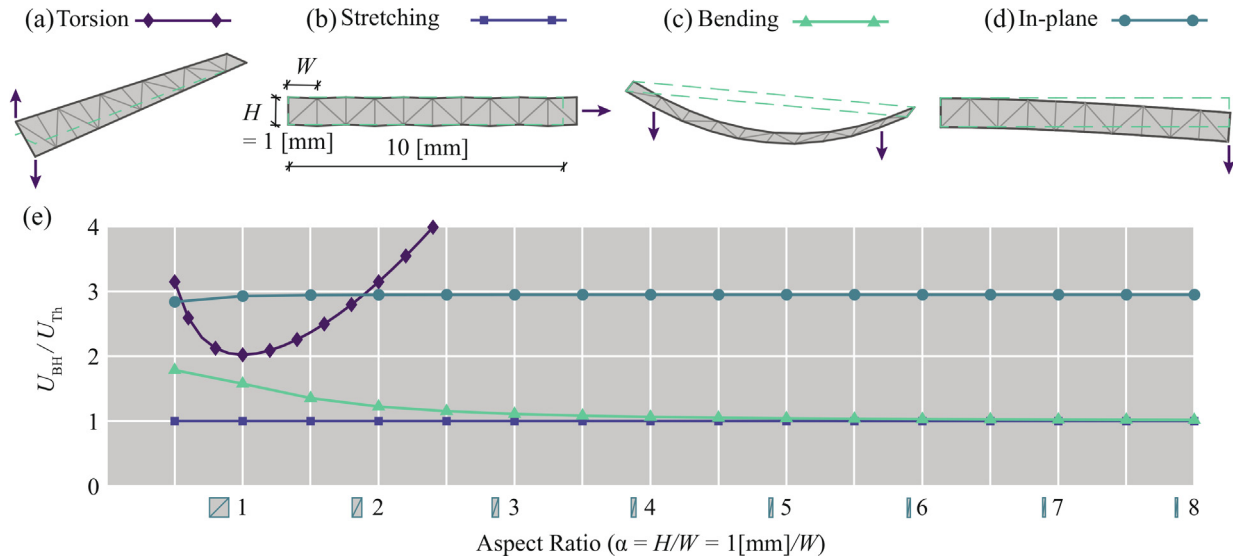


**Fig. 5.** To verify the stiffness expressions for the bar and hinge model, a long, thin strip was modeled and loaded in four ways: (a) torsion, (b) stretching, (c) bending out-of-plane, and (d) bending in-plane (deformations are exaggerated 1,000 times). (e) The strain energy in the bar and hinge model,  $U_{BH}$ , compared to the strain energy based on structural mechanics theory,  $U_{Th}$ , with respect to the mesh aspect ratio,  $\alpha$ .

The first loading case represents torsion in the strip. At one end, the nodes are restrained in the  $x$ -,  $y$ -, and  $z$ -directions. At the other end of the strip, one node is pulled up and the other is pulled down by a prescribed displacement of  $5 \times 10^{-4}$  [mm] (see Fig. 5(a)). The second loading case represents tension along the long axis of the strip. One end of the model is restrained in the  $x$ -,  $y$ -, and  $z$ -directions and the other end is loaded in tension along the plane of the sheet, again with a prescribed displacement of  $5 \times 10^{-4}$  [mm] (see Fig. 5(b)). The third loading case represents out-of-plane bending of the strip where both ends are simply supported and the nodes adjacent to the ends are loaded in the downward direction, similar to a four point bending test (see Fig. 5(c)). The last loading case represents in-plane bending where one end of the strip is restrained in the  $x$ -,  $y$ -, and  $z$ -directions and the other end is loaded perpendicular to the long axis of the strip similar to a cantilevered beam (see Fig. 5(d)).

The energy in the bar and hinge model,  $U_{BH}$ , is calculated by summing the strain energy in the bending hinges and bars after loading. Each of the four loading cases has a structural mechanics solution for the strain energy which we calculated based on the geometry and material properties of the strip. We call this analytically calculated energy the theoretical energy,  $U_{Th}$ . We compared the bar and hinge energy to the theoretical energy for each loading case at different aspect ratios. From Fig. 5(e), we see that in torsion, the bar and hinge model overestimates the energy (and stiffness) compared to the structural mechanics solution. At an aspect ratio of one ( $\alpha = 1$ ), where the height of each triangular panel is equal to its width, the bar and hinge energy achieves its minimum strain energy solution, which is roughly double that of the theoretical solution. In this minimum torsion case,  $\alpha = 1$  and the bending hinges align with the  $45^\circ$  axis. This hinge orientation most closely aligns with the deformation from real torsion and thus gives the closest approximation. For other aspect ratios, the diagonal bars in the bar and hinge model do not align with the real torsion deformation, and high-energy bar straining occurs. For loading cases where torsion is present, the bar and hinge model will overestimate the stiffness of the structure (see Section 5.2 for an example).

Because the unit truss model is used to derive the tensile stiffness definition in Section 3.1, we see that the strip in tension matches the theoretical solution for all aspect ratios. These results

are encouraging for post-fold loading modeling of the structure because loading deformations often include stretching.

For out-of-plane bending, we see that the result depends on the aspect ratio of the bar and hinge model. For low aspect ratios (that is, coarser meshes), the bending hinges overestimate the stiffness of the sheet. However, as the aspect ratio increases, the strain energy approaches the theoretical solution. Aspect ratios over three ( $\alpha > 3$ ) will give out-of-plane bending solutions within 10% of the theoretical value. Aspect ratios over four ( $\alpha > 4$ ) will give solutions within 5%. Because bending deformations dominate the folding behavior of curved-crease origami, we expect better overall folding results with a finer mesh that still has a convergent solution.

Finally, for in-plane bending, we see that the bar and hinge model overestimates the stiffness of the sheet by a factor of about three. This is due to the discrepancy between the theoretical stress distribution across the cross-section of the sheet and the bar and hinge's treatment of stress as concentrated bar forces. The factor of three can also be back-calculated from the initial bar definitions in Eqs. (3)–(5). This increased stiffness should not affect the folding of curved-crease models because shear is rarely present; however, it might become important in post-fold loading of the structure. For structures where in-plane bending is dominant, the bar areas can be reduced by three to get the bar and hinge model to approach theory. However, because in-plane bending is coupled with stretching, such a reduction will result in underestimating the stretching stiffness by the same factor of three.

Overall, these strip tests show the benefits and limitations of the bar and hinge model as formulated here. For folding of the models where low-energy bending deformations dominate, the model will capture the final shape and stiffness well. For analyzing the behavior of structures after folding, some user discretion must be applied to ensure that the results are accurate. For cases where torsional deformations of the system are expected, an aspect ratio of  $\alpha \approx 1$  should be used and stiffness may still be overestimated by a factor of two. For cases with global in-plane bending deformation, the user could assume that the stiffness will be overestimated by a factor of about three.

When modeling most other curved-crease origami, the analyst should choose a moderate aspect ratio. Through experience with

modeling various geometries, the recommended range for the aspect ratio is  $\alpha \in [5, 12]$ . In this range, the mesh is fine enough to properly approximate the curved geometry of the creases and will meet the theoretical stiffness for stretching, shearing, and out-of-plane bending. Additionally, such a range will give solutions that reliably converge (although the model will converge for  $\alpha \leq 30$ , depending on the geometry, boundary conditions, loading conditions, and increment size). Although it is possible to modify the bending stiffness definition in Section 3.2 to converge to theory for  $\alpha < 5$ , such a task would not benefit analysis of most curved-crease origami and is beyond the scope of this paper.

**Supplementary codes** provided along with this publication include full implementations of the bar and hinge model for curved-crease origami. A modified version of the code that simulates only a strip is provided for the tensile case shown in Fig. 5(b).

#### 4.2. Bending a creased annulus sector into a theoretical cone

A small subset of curved-crease origami structures can be described as a piece-wise combination of well-defined geometric surfaces, such as cones, cylinders, and tangent developable surfaces connected at a single crease (Duncan and Duncan, 1784). The non-zero principal curvature,  $\kappa_2$ , of these developable surfaces can be calculated and included along with the bending modulus of a sheet,  $D_b = Et^3/(12[1 - \nu^2])$ , in a theoretical strain energy expression,  $U_{\text{Th}} = 1/2 \int_A D_b \kappa_2^2 dA$ . Using the theoretical strain energy of the surface as a point of comparison to the bar and hinge model, we can examine the performance of the model.

A potential candidate for a simple, piece-wise developable structure is a circular annulus sector folded about its center (see Fig. 6(a)). If the structure is restrained in a specific way, we can use differential geometry to show that the deformed midsurface of the folded sheet is a portion of a cone with well-defined, non-zero principle curvature.

Suppose we have a thin, elastic sheet with thickness,  $t$ , and elastic modulus,  $E$ , that is cut into the shape of a circular annulus sector with width in the radial direction,  $2w$ , and a sector angle of  $\zeta_0$  (see Fig. 6(a)). We prescribe a parametric, flat crease,  $\mathbf{c}_0(t)$ , into the sheet such that the crease is always parallel to edges of the sheet that follow the polar direction. This crease is a circular arc with radius of curvature,  $R_0$ , placed evenly between the inner and outer radial edges of the sheet (that is, the distance between the crease and the inner and outer radial edges is  $w$ ).

The flat crease has curvature,  $\kappa_0$ , constant along its length. After folding to some dihedral angle,  $\phi \in (0, \pi)$  [rad], constant along the length of the curve, the deformed crease,  $\mathbf{c}_f(t)$ , remains planar using structural restraints (in the  $z$ -direction), and has a different curvature,  $\kappa_f$ , and radius of curvature,  $R_f = 1/\kappa_f$  (see Fig. 6(b)). The crease lies in one osculating plane (that is, the plane in which the tangent and normal vectors at all points along the crease lie). The angle between the surface of the osculating plane and the midsurface of the sheet to the left of the crease is  $\eta_L$  and is related to the dihedral angle by  $\eta_L = (\pi - \phi)/2$  (see Fig. 6(c)). By definition, the torsion of the deformed, planar crease,  $\tau$ , is zero everywhere. Additionally, because the fold angle is constant, the angle  $\eta_L$  does not change along the length of the crease.

Fuchs and Tabachnikov (1999) proved that the curvature of the deformed crease can be calculated with  $\kappa_f = \kappa_0 / \cos \eta_L = \kappa_0 / \sin(\phi/2)$ . Then, with added consideration for curve speed,  $|\mathbf{c}'_f(t)|$ , Lang et al. (2017) confirmed that the angle,  $\gamma_L$ , between the crease tangent and the generators of the curved sheet's midsurface,  $\mathbf{g}_L(t)$ , is defined by

$$\cot \gamma_L = \frac{\eta'_L / |\mathbf{c}'_f(t)| + \tau}{\kappa_f \sin \eta_L} = \frac{-\phi' / (2|\mathbf{c}'_f(t)|) + \tau}{\kappa_0 \cot(\phi/2)}. \quad (13)$$

The generators represent rulings on the curved, developable surfaces and coincide with the direction of zero principle curvature,  $\kappa_1 = 0$ . By definition, the non-zero principle curvature of the surface is orthogonal to the generators in the neighborhood of the crease. Additionally, the layout of the generators (defined by  $\gamma_L$ ) tells us the geometric properties of the surface.

If we apply all the assumptions and calculations made for the circular creased annulus sector, Eq. (13) reduces to  $\cot \gamma_L = 0$  for  $\phi \in (0, \pi)$  [rad]. This new equation has the solution  $\gamma_L = \pi/2$  [rad]. Thus, the generators of this creased annulus are normal to the crease at all points. These generators coincide with the direction of curvature,  $\kappa_f$ , and meet at one point (the apex), and the folded shape is identical to a segment of a cone (see Fig. 6(b) and (d)). A similar process can be used to show that the generator angles to the right of the crease,  $\gamma_R$ , are also perpendicular to the crease. As shown in Fig. 6(d and e), the creased annulus sector coincides with a portion of a cone with the upper portion and apex reflected about the osculating plane of the crease. This observation is consistent with Mitani's method for planar, curved folding in (Mitani and Igarashi, 2011).

The non-zero principal curvature of a right cone is calculated as

$$\kappa_2(u) = \frac{1}{\tan(\phi/2)u\sqrt{1 + \tan^2(\phi/2)}}, \quad (14)$$

where  $u$  is the distance from the apex of the cone extending down through the center (see Fig. 6(e)) (Weisstein, 2019).

We used the bar and hinge method to model the creased annulus sector made with different sector angles (see Fig. 6(f) i–iv). The bending and stretching energy of these models,  $U_{\text{BH}}$ , is plotted for different aspect ratios and normalized by the theoretical cone energy,  $U_{\text{Th}}$  (see Fig. 6(f)). The aspect ratio is defined as the mean aspect ratio of all the triangular panels as defined earlier. For coarser meshes with low aspect ratios, the bar and hinge model overestimates the energy and stiffness of the sheet. As the mesh size decreases, the energy in the bar and hinge model approaches the theoretical solution. For models with an aspect ratio greater than seven ( $\alpha > 7$ ), the bar and hinge solution is within 10% of the theoretical solution. For sufficiently high aspect ratios, we see that the bar and hinge energy dips below the theoretical solution. Underestimating the theoretical cone energy is consistent with finite element solutions of the same problem carried out in Woodruff and Filipov (2018). The energy underestimation indicates that the bar and hinge model is capable of capturing some of the end effects (also called the “free edge effect” (Lee et al., 2018)) where the unsupported edges of the curved-crease annulus sector do not achieve the curvatures of a pure cone (Badger et al., 2019).

This model is also available in the [Supplementary code](#).

#### 4.3. Laser scanning verification of complex curved-crease origami

For certain curved-crease origami patterns, there is no existing theoretical description of the deformed shape. Kinematics and elasticity formulations alone cannot give the surface shape between two curved creases unless the pattern is highly constrained, for instance, using a tessellation of creases (Lee et al., 2018). Additionally, theories of developable surfaces used to verify the deformed shape of the creased annulus sector in Section 4.2 become complicated for surfaces that are neither conical or cylindrical, called tangent developable surfaces. Understanding the shape of this general tangent developable surface requires parameters such as generator angles that are not apparent given the flat fold pattern. A recent method by Badger et al. (2019) finds the natural shape of general developable surfaces using an energy minimization method. However, this method is limited to finding the energy minimal case when only one crease is used on the pattern.

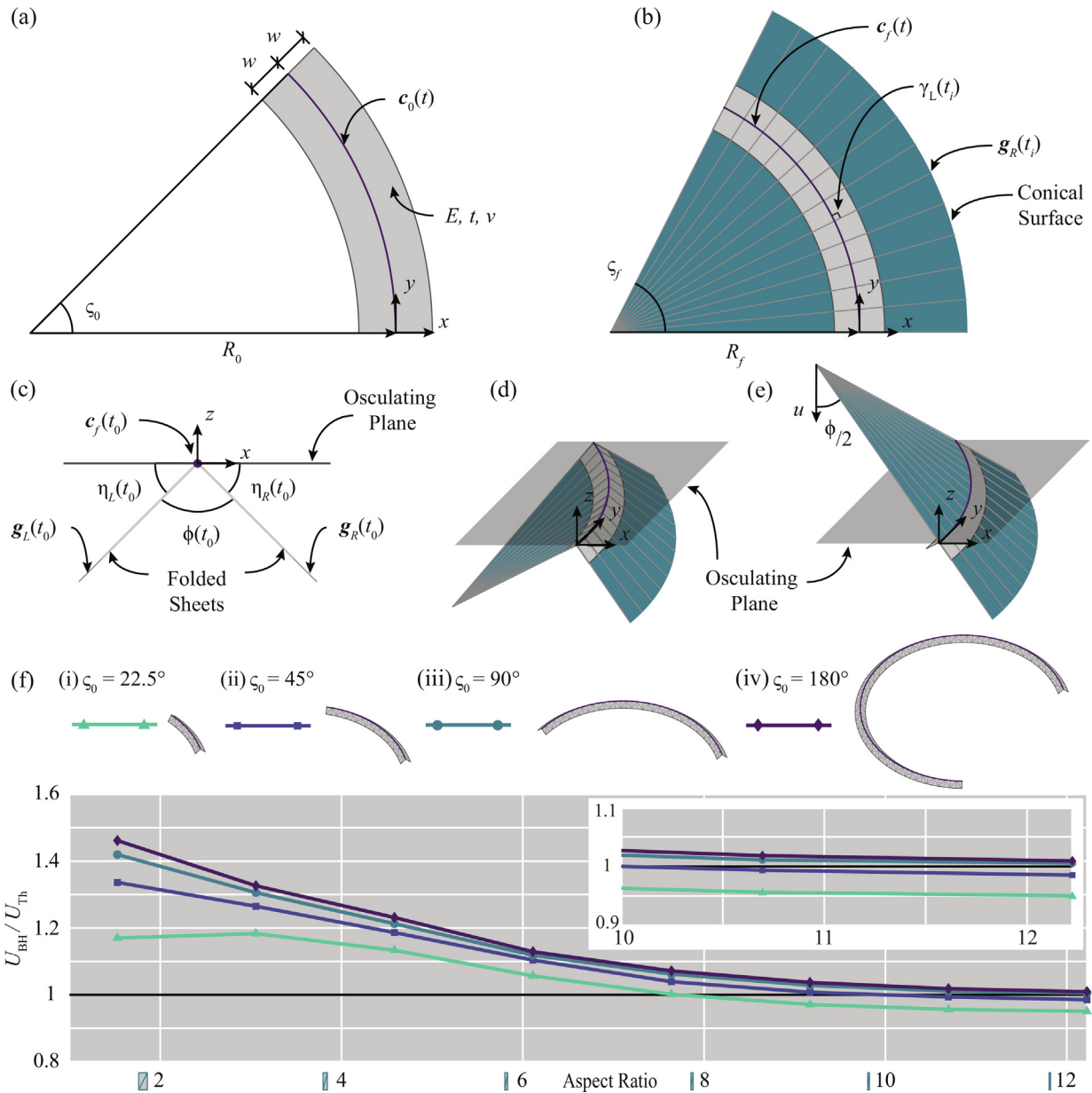


**Fig. 6.** (a) Illustration of the parameters for a flat, circular annulus sector creased about its mid-radius. (b) Top-view illustration of the parameters for the same circular annulus sector that has been folded. (c) Illustration of the cross-section at some point,  $t_0$ , along the length of the folded curve with additional parameters. (d) The creased annulus sector coincides with portions of a cone. (e) When the upper portion of the cone is reflected about the osculating plane touching the crease, the conical shape of the origami structure becomes clearer. (f) A comparison of the bar and hinge strain energy,  $U_{BH}$ , with the strain energy of a cone,  $U_{Th}$  for (i–iv) four different flat sector angles,  $\zeta_0$ .

The bar and hinge method implicitly accomplishes energy minimization; thus, comparison between the previous methods would be either unrealistic (e.g., requiring, a priori, assignment of generator angles) or trivial given an appropriate mesh size. Instead, we verified the deformed shapes of complex models by comparing them with the shapes of physical paper models. The process of capturing and comparing the folded shape of a paper model is shown in Fig. 7(a). Starting from a flat, curved-crease fold pattern, we fabricated the physical model from sturdy, 0.274 [mm] thick, linen paper. All models are about 10 [cm] by 10 [cm] when flat. We cut the pattern using a laser cutting machine, and we hand-folded the model such that the crease material yields and the model holds some natural rest angle. Using a NextEngine 3D Laser Scanner HD machine, we captured the deformed shape of the paper model with an accuracy of 0.127 [mm] (0.005 [in]) and at a resolution of 10,400 [points/cm<sup>2</sup>] (67,000 [points/in<sup>2</sup>]), which is the highest quality scan available. From the scan, a set of points with

position values in three-dimensional Cartesian coordinates, called the point cloud, is saved and used in the comparison. We chose to sample every fifth point in the point cloud to expedite analysis (the largest unprocessed point cloud included about 250,000 points).

Simultaneously, we modeled the same system with the bar and hinge model using the paper’s material properties and the geometry of the fold pattern. The prescribed fold angle was estimated from the point cloud, and various  $L^*$  values were tested to find the result giving the lowest mean error (see Section 4.4). To represent the shape of the surface between the creases in the bar and hinge folded model, we enrich the mesh by adding points along the length of each bar. We then chose three points from the point cloud and three corresponding points from the enriched mesh to align the two systems (usually, three easily identifiable locations such as corners or crease ends). After alignment, for each point in the enriched mesh, we found the closest point in the point cloud

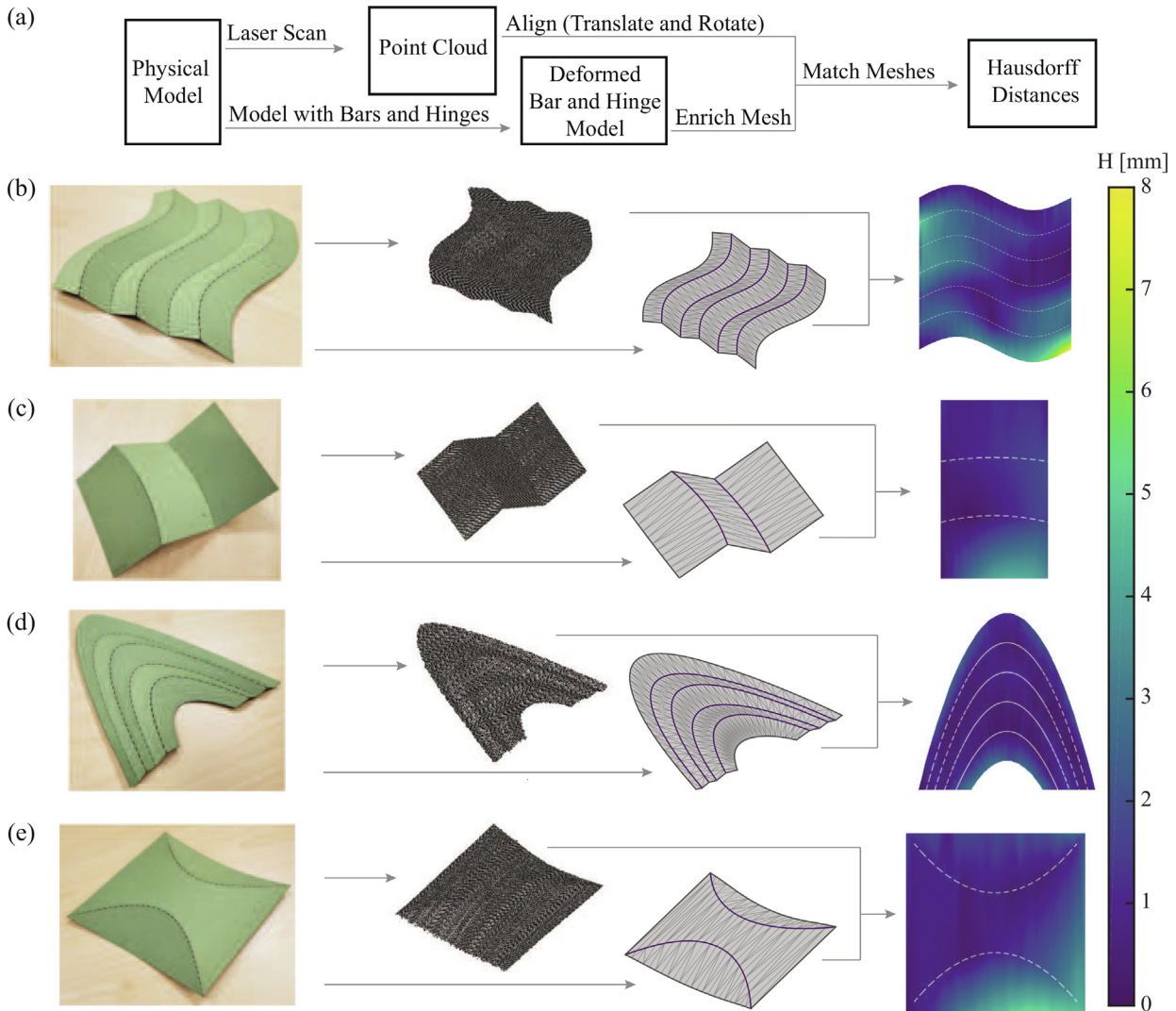


**Fig. 7.** The accuracy of the bar and hinge model was assessed by comparing the simulated deformed shape to the shape of folded paper models measured using laser scanning. (a) The analysis process starting with a physical model leading to a plot showing the Hausdorff distances at each node on the bar and hinge enriched mesh. Four examples of complex curved-crease origami are shown, including (b) a sine wave tessellation, (c) a rectangular sheet with two circular arc creases of different radii, (d) a canopy made from repeated parabolic creases, and (e) a square with two parabolic creases in opposite directions.

and calculated the distance between them. This distance is the Hausdorff distance of that point.

We plotted the Hausdorff distances of each point in the enriched bar and hinge mesh and calculated simple statistical values (mean distance, standard deviation of distances, and the median distance). The sine wave tessellation (Fig. 7(b)) has an average Hausdorff distance of less than 2 [mm], and all other examples have an average Hausdorff distance less than 1 [mm]. We see in the far-right images in Fig. 7(b–e) that the deformed shapes of the bar and hinge models agree with the physical models. The largest errors, about 8 [mm], occur at edges and are mainly caused by human errors in choosing the alignment points or are due to local deformations not captured by the bar and hinge model. We see from these comparisons that the bar and hinge model is capable of approximating the deformed shape of complex folded curved-crease origami structures.

#### 4.4. The effect of rest angle and fold stiffness on the geometry

As shown in Eq. (1), the in-plane, sheet bending, and the crease folding energy all contribute to the energetic equilibrium of the

structure. The crease folding energy is a function of the fold stiffness,  $k_f$ , as well as the difference between a prescribed rest angle,  $\phi_R$ , and the actual fold angle of the crease,  $\phi$ . The fold stiffness is inversely proportional to the length scale parameter,  $L^*$ , which is prescribed in the bar and hinge model. To fold the origami into a three-dimensional state, we sequentially reduce the rest angle from  $\phi_R = 180^\circ$ , downward. For curved-crease origami, any folded state results in elastic bending energy stored in the sheet. This elastic energy is counteracted by elastic folding energy in the creases. Thus, in any folded state,  $\phi_R \neq \phi$ , the difference between the prescribed and actual fold angles depends on the prescribed length scale parameter,  $L^*$ , which factors into the fold stiffness. As discussed in Section 3.3, there is no straightforward method for determining the value of  $L^*$ . Instead, here we explore how this value affects the overall folded geometry.

In Fig. 8, we explore the folded geometry of two structures: a creased annulus sector and a rectangular sheet with two curved folds of different, uniform curvature. Different values of  $L^*$  are used to define the fold stiffness, and the systems were analyzed by decreasing the rest angle of the crease. High values of  $L^*$  indicate a flexible fold, while low values indicate a stiffer fold. Previous

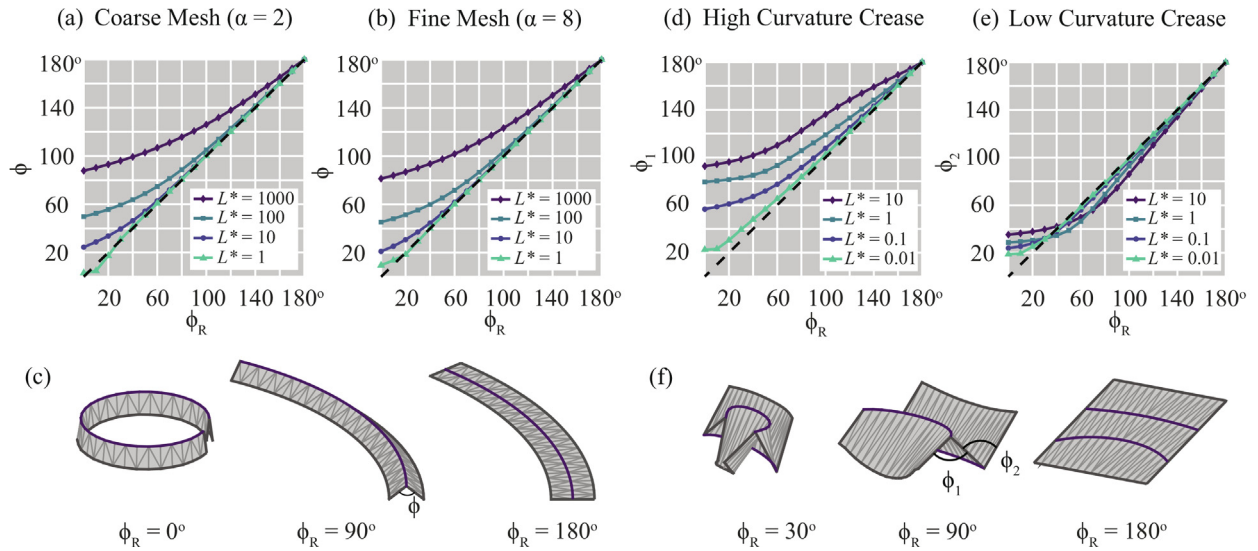


**Fig. 8.** The value for folding length scale,  $L^*$ , and the prescribed fold angle,  $\phi_R$ , both affect the folded geometry of curved-crease origami. The actual crease angle versus the rest angle for a creased annulus sector with (a) a coarse mesh and (b) a fine mesh, for different values of  $L^*$ . (c) The deformed shapes with three prescribed angles and  $L^* = 1$ . (d and e) The actual crease angle versus the prescribed fold angle of a rectangular sheet with two curved creases with different curvatures uniform along their lengths. (f) Deformed shapes with  $L^* = 0.01$ .

research has shown that for origami,  $L^*$  can be assumed to be in the range of 25 [mm] to 100 [mm], while experimental results on folds have varied from 1 [mm] to 700 [mm] (Filipov et al., 2017).

We first study the behavior of the curved-crease annulus sector which was introduced in Section 4.2. Comparing Fig. 8 (a) and (b), we see that the mesh discretization does not have a significant influence on achieving the prescribed fold angle. Furthermore, the fold angle,  $\phi$ , tends to be close to the rest angle when realistic values of  $L^*$  are used, and when  $\phi_R > 90^\circ$ . As expected, when  $\phi_R$  is reduced further, the rest angle and the actual fold angle deviate. An exception is the stiffest folds ( $L^* = 1$ ) which essentially restrains the annulus to take the prescribed fold angle. Lang et al. (2017) predicts that as the dihedral angle approaches zero, the nonzero principal curvature of the sheet about the crease asymptotically increases towards infinity. Our results further verify this observation by showing that all systems have some finite deviation from  $\phi_R = 0^\circ$ . The study of the curved-crease annulus sector shows that for simple, single-crease systems, the folded state is not highly dependent on the choice of  $L^*$ , and an approximate folded state can be achieved by defining the rest angle,  $\phi_R$ . Furthermore, the same folded geometry (angle  $\phi$ ) can be achieved with different combinations of  $L^*$  and  $\phi_R$ .

The curved-crease origami with two folds of different, uniform curvature exhibits a more varied response when  $L^*$  is changed (see Fig. 8(d and e)). In addition to the counteraction between crease folding energy and sheet bending energy, here the incompatibility between the crease curvatures also affects the folded state. The crease with low curvature (that is, the straighter crease with fold angle  $\phi_2$ ) tends to stay close to the prescribed rest angle regardless of  $L^*$ . On the other hand, the crease with high curvature can only approach the rest angle when the crease is much stiffer than a realistic origami system ( $L^* = 0.01$ ). In reality, this would correspond to using a mechanical system to restrain the crease. For realistic values of  $L^*$  (e.g.,  $L^* = 10$ ), the crease with higher curvature,  $\phi_1$ , deviates from the prescribed fold angle which indicates that there is more counteraction between energies in the system. From these case studies, we see that the value for  $L^*$  can have a more significant influence for more complex curved-crease origami, and choosing an appropriate value of  $L^*$  is problem-specific (for example, affected by differential curvature of folds in the pattern). A user

could perform similar parametric studies by varying both  $\phi_R$  and  $L^*$  to find the combination that gives a reasonable approximation of the folded structure. As shown in the next section, finding a reasonable approximation of the folded geometry is important before moving on to post-fold loading problems.

## 5. Modeling the anisotropy of curved-crease structures

The unique structural properties of curved-crease origami come from their folded geometry and post-folding behavior. Specifically, folded curved-crease origami will resist loads and store energy differently depending on the direction of loading. We describe this behavior as global stiffness anisotropy of the structure, or simply, anisotropy. With the inclusion of variable parameters such as the fold angle or post-loading deformed shape, the anisotropy takes on a new dimension and can be functionally tunable. For engineering applications, this anisotropy can be used to create structures which are stiff enough to support loads in one direction, but can deform and fold in a prescribed fashion when loaded in other directions. Curved-crease geometries can also reduce anisotropy in structures like corrugations by varying the direction of the creases (Woodruff and Filipov, 2020).

The bar and hinge model seems to be well-suited for exploring this anisotropy because it can simulate different boundary conditions and load cases, it converges reliably, and can provide relatively accurate results when considering global structural behavior. Moreover, the model is numerically efficient which allows for parametric studies on the anisotropy and future optimization of these unique behaviors. The bar and hinge formulation presented in Section 3 limits the number of user-specified parameters (for example,  $L^*$ ) which makes the system behavior directly dependent on geometric and material properties which greatly simplifies a user's role in an optimization process. Furthermore, Fig. 8 suggests that linear variations in  $L^*$  result in smooth variations in the structural response. We also expect that other linear variations in geometry and materials would result in smooth behavior variations, allowing for convex functions in different parametric optimizations. In this section, we use the bar and hinge model to study the anisotropy of two curved-crease origami

structures after folding and use these studies to evaluate the capabilities and limitations of the method.

### 5.1. Multi-directional stiffness of a cantilevered creased annulus sector

The creased annulus sector described in Section 4.2 has interesting anisotropy despite being made with only a single crease. We looked at the stiffness of this geometry when it is folded to different fold angles, restrained at one end, and loaded at the other end (see Fig. 9(a)).

The tip of the structure is loaded in different directions denoted by the spherical coordinate system with  $\varphi$  as the polar angle (that is, the angle to the  $z$ -axis) and  $\vartheta$  as the azimuthal angle (that is, the angle to the  $x$ -axis). A small displacement analysis is performed. After loading, the resultant forces acting on the structure,  $F$ , is calculated in the same direction as the applied displacement,  $\Delta$ , and these two quantities are used to calculate the stiffness,  $K = F/\Delta$ . Fig. 8(b–e) show the results of this analysis for four folded states of the creased annulus sector, represented by the fold angle,  $\phi \in \{180^\circ, 150^\circ, 120^\circ, 90^\circ\}$ .

We see that in all folded states, the stiffest loading directions are in the plane of the creases where  $\varphi = 90^\circ$ . When the sheet is flat ( $\phi = 180^\circ$ ), there is high stiffness for any in-plane loading (that is, the  $x$ - $y$  plane where  $\varphi = 90^\circ$ ). As the structure starts to fold out-of-plane, it also gains stiffness in other azimuthal ( $\vartheta$ ) directions. Two distinct points with high stiffness emerge at  $\vartheta \approx 80^\circ$  and  $260^\circ$  when  $\varphi = 90^\circ$ . These points correspond to directions of loading that are nearly parallel to the crease at the tip (that is, the  $y$ -axis as shown in Fig. 9(a)). These directions and regions change slightly as the system is folded. The regions with higher non-orthogonal and out-of-plane stiffness increase in domain size with more folding (that is, the eccentricity of the ellipses of high stiffness lowers and becomes more circular with increased folding).

This model is also available in the [Supplementary code](#).

### 5.2. Large deformation response of a cantilevered, creased annulus sector

We continue the analysis above by loading the creased annulus sector in the upward direction and exploring the large deformation

response. Fig. 10(a) shows the deformed shapes of a physical model of the creased annulus sector made from paper. From these pictures, we see that the global deformation includes torsional bending of the thin sheet. In Section 4.1, we found that the proposed formulation for the model overestimates torsional stiffness in thin strips of material. This overestimation varied with the mesh size, and a minimal error occurred when the aspect ratio of the panels is one.

For a structure such as this creased annulus sector, the effects of stretching, shearing, bending, and torsion all play a part in this large, upward deformation. Assigning a mesh with an aspect ratio of one will give poor results in bending and shearing (that is, will overestimate the stiffness), but an aspect ratio of eight will give poor results in torsion. We first explored the deformed shape of these two mesh discretizations by subjecting the creased annulus sector to a displacement-controlled simulation. Fig. 10(b) shows that the coarser mesh ( $\alpha = 1$ ) can capture more twisting about the fold than the finer mesh ( $\alpha = 8$ ) shown in Fig. 10(c). Furthermore, Fig. 10(d) shows that the finer mesh ( $\alpha = 8$ ) has a significantly stiffer load-deformation response. Moreover, the coarse mesh ( $\alpha = 1$ ) gives the lowest stiffness and force response. From our preliminary analysis with this model, the lowest stiffness solution would also be the most accurate when compared to the real-world behavior. Fig. 10(e) and (f) show the strain energy of different elements for the coarse ( $\alpha = 1$ ) and fine ( $\alpha = 8$ ) meshes, respectively. Both cases have a high proportion of bar stretching energy which is expected for this type of non-conforming vertical displacement. The coarser mesh has a substantially lower total energy, and both the sheet bending and crease folding contribute to the total system energy. These element deformations are essential for capturing the global torsion of the structure. The finer mesh has about the same magnitude of crease folding energy; however, it overestimates the bending and stretching energy in global torsion.

For problems with large twisting, the bar and hinge model can give a reasonable approximation of the true deformed shape. However, the forces and stiffness in the load-deformation response will likely be overestimated. A user of this model who is analyzing a structure and load case with high torsion should consider using different aspect ratios to identify which case gives the lowest

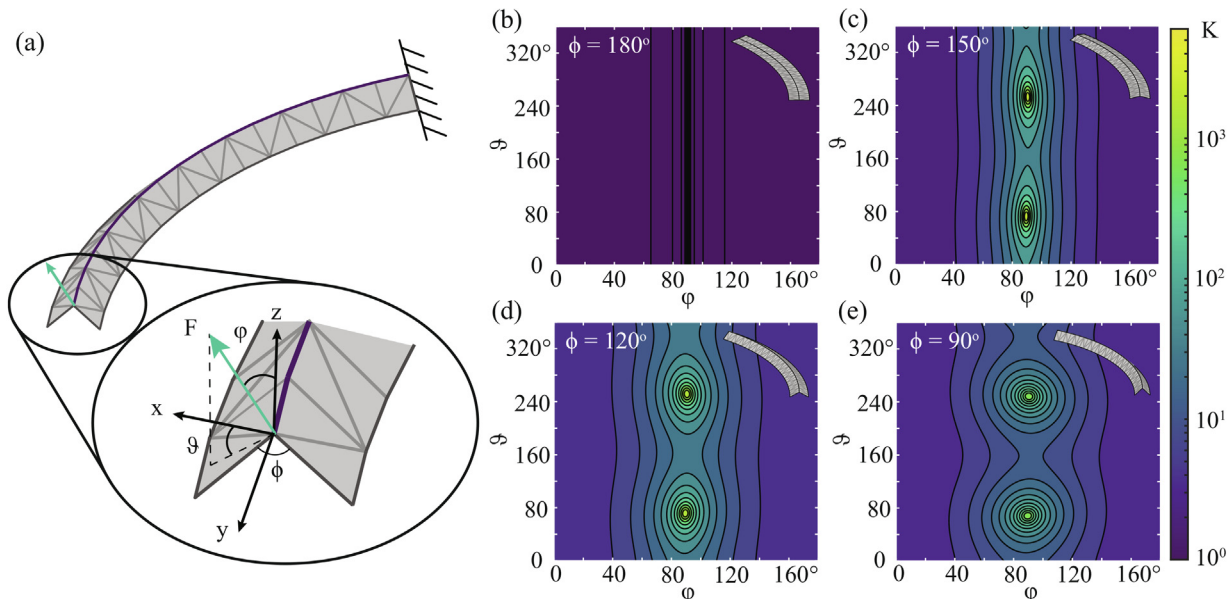
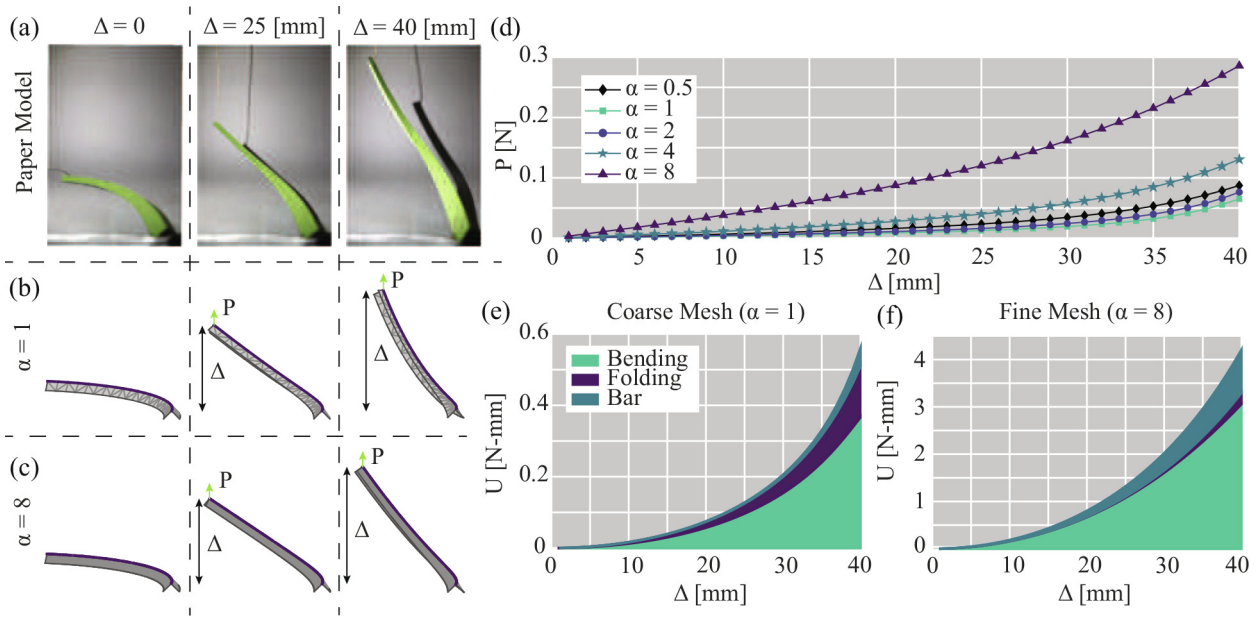


Fig. 9. (a) A creased annulus sector is fixed at the right end and loaded with a point load on the left. The point load is applied in different directions defined by spherical coordinates,  $\vartheta$  and  $\varphi$ . (b–e) The stiffness,  $K$ , for different loading directions (that is,  $\vartheta$  and  $\varphi$ ) is shown for four different fold angles of the structure,  $\phi$ .



**Fig. 10.** When the creased annulus sector is subjected to an upward displacement, the large displacement response includes torsional deformations. (a) A physical model made from paper. Bar and hinge simulations with (b) a coarser mesh ( $\alpha = 1$ ) capture the torsional displaced shape better than (c) a finer mesh ( $\alpha = 8$ ). (d) The load-deformation plot of five models with different mesh discretizations. The energy distribution of (e) the coarse mesh has lower bending and bar energy than (f) the finer mesh under the same displacement.

forces and energy. This case will likely have a low aspect ratio and would provide the approximation closest to reality.

### 5.3. Anisotropy of a pinched fan

One curved-crease origami structure with novel potential for engineering use is a folded fan made with pleated creases that is pinched after folding (see Fig. 11(a–d)). This model has a low rotational stiffness about the pinched point and large stiffness in the direction of the creases. Such a system could be used to create rotational hinges with variable and programmable stiffness with potential applications in robotics, architecture, and beyond.

Here, we quantify the difference between rotational and axial stiffness for this structure by performing a deformation-controlled analysis using the bar and hinge model. The axial stiffness,  $K_a$ , is computed from a point load applied into the middle crease line,  $P_a$ , while the rotational stiffness,  $K_r$ , is obtained from a point load,  $P_r$ , that is orthogonal to the same crease. The fan is supported through its center in the  $x$ - and  $z$ - directions with an additional  $y$ -restraint at the lowest node on the support line (see Fig. 11(a)). The analysis was performed over two separate regimes. The first regime involved folding the flat pattern into the three-dimensional fan shape with fold angles of  $90^\circ$ . The next regime involved pinching the folded fan in the center to create the rotating hinge. During the pinching process, we encountered a case where sequential folds in the pattern buckle together similar to other origami pleats in the literature (Filipov and Redouty, 2018). Each of the analysis regimes was divided into 100 displacement increments, and the axial and rotational stiffness were calculated at each increment (Fig. 11(e)).

For all increments, the axial stiffness is greater than the rotational stiffness. Fig. 11(f) shows the ratio of the rotational stiffness to the axial stiffness. As the model is pinched, this ratio decreases indicating a larger difference between the rotational and axial stiffness. At the final increment, the rotational stiffness is about 0.2% that of the axial stiffness which indicates the formation of a rotational hinge in the structure. If the pinching on the structure is released, then system will recover to a state with higher rotational

stiffness. This type of stiffness anisotropy in curved-crease origami could be exploited for creating joints and structures with tunable characteristics.

## 6. Concluding remarks

In this paper, we have introduced a bar and hinge method for simulating the structural behavior of curved-crease origami during and after folding. This method is rapid and can model a variety of curved-crease origami structures with different boundary conditions. There are three element types, including in-plane bars, bending hinges, and folding hinges, which together can capture the global stiffness of the structure. We derived the stiffness values of each element based on the system geometry, the mesh discretization, and material properties.

The stiffness expressions were verified and explored using different theoretical and empirical models of simple and complex curved-crease origami structures. The first verification method compared the deformation response of long strips of material modeled using the bar and hinge method to theoretical solutions from structural mechanics. The stiffness expressions were also verified using differential geometry solutions and by comparing the deformed shape of paper models to bar and hinge models through laser scanning. The influence of choosing a rest angle and a fold stiffness were also explored in relation to the final folded shape.

The method can be used to explore the complex, post-fold stiffness anisotropy of various curved-crease origami structures. We first showed a cantilevered creased annulus sector that has regions of high stiffness which correspond to loading parallel to the fold lines. The out-of-plane stiffness of this structure increases as it becomes more folded. When the cantilevered annulus sector is loaded upward, it experiences a complex, torsional deformation. We also explored a curved-crease fan for its stiffness parallel and perpendicular to the fold lines. This structure shows a tunable anisotropy where a rotational hinge can be created and tuned by pinching the center of the fan.

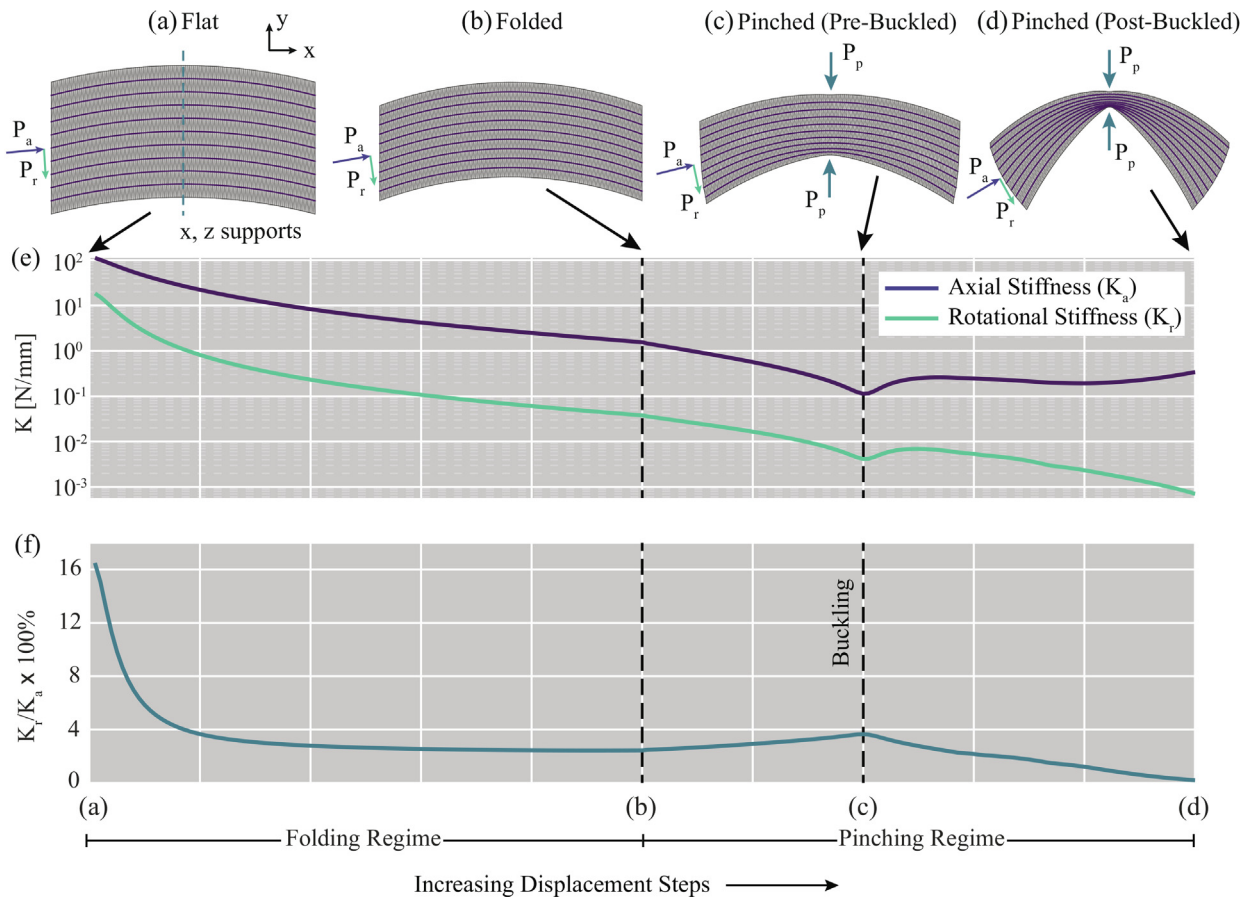


**Fig. 11.** The deformation and stiffness of a curved-crease origami fan was modeled with the bar and hinge method. The structure was folded in the first regime (a and b) and is subsequently pinched in the second regime (c and d). (e) The rotational and axial stiffness of the structure changes during the two regimes. (f) The ratio of rotational to axial stiffness drops as the structure is pinched indicating the formation of a hinge.

Our exploration of this new formulation of the bar and hinge model shows that it is well suited for capturing the folding sequence of curved-crease origami. Because the folding primarily engages sheet bending, the deformed shape and stiffness can be captured well with moderately fine mesh discretization sizes ( $\alpha \in [5, 12]$ ). Stretching and shearing stiffness is captured well by the model; however, the stiffness of in-plane bending is overestimated by a factor of three, regardless of the mesh. This stiffness overestimation can be reduced by reducing the bar stiffness by a third – though, a threefold reduction in stretching stiffness would also occur. The bar and hinge model can approximate global torsional deformations, but typically overestimates stiffness for this behavior. Coarser meshes tend to perform better when high levels of torsion occur. These preliminary studies show how curved-crease origami structures can be used to create novel mechanical behaviors such as anisotropic stiffness and tunable stiffness properties.

Example code is provided as [Supplementary material](#) with various examples of curved-crease origami folding and post-fold loading simulations. We hope that this code and the bar and hinge model in general will help expedite research on the engineering applications of curved-crease origami by providing a fast and reasonably accurate simulation tool for the folding and post-folding structural behavior.

#### Declaration of Competing Interest

The authors declare that they have no known competing financial interests or personal relationships that could have appeared to influence the work reported in this paper.

#### Acknowledgments

The authors are grateful for the financial support provided by the Office of Naval Research (Grant No. N00014-18-1-2015). The first author is also thankful for support from the National Science Foundation Graduate Research Fellowship Program (Grant No. DGE 1256260).

#### Appendix A. Supplementary data

Supplementary data associated with this article can be found, in the online version, at <https://doi.org/10.1016/j.ijisolstr.2020.08.010>.

#### References

- Badger, J.C., Nelson, T.G., Lang, R.J., Halverson, D.M., Howell, L.L., 2019. Normalized coordinate equations and an energy method for predicting natural curved-fold configurations. *J. Appl. Mech.* 86 (7). <https://doi.org/10.1115/1.4043285>.
- Beex, L.A.A., Peerlings, R.H.J., 2009. An experimental and computational study of laminated paperboard creasing and folding. *Int. J. Solids Struct.* 46 (24), 4192–4207. <https://doi.org/10.1016/j.ijisolstr.2009.08.012>.
- Bende, N.P., Evans, A.A., Innes-Gold, S., Marin, L.A., Cohen, I., Hayward, R.C., Santangelo, C.D., 2015. Geometrically controlled snapping transitions in shells with curved creases. *Proc. Natl. Acad. Sci. U.S.A.* 112 (36), 11175–11180. <https://doi.org/10.1073/pnas.1509228112>.
- Demaine, E.D., Demaine, M.L., Koschitz, D., Tachi, T., 2011. Curved crease folding - a review on art, design and mathematics. In: *Proceedings of the IABSE-IASS Symposium: Taller, Longer, Lighter, London, England*.
- Dias, M.A., Dudte, L.H., Mahadevan, L., Santangelo, C.D., 2012. Geometric mechanics of curved crease origami. *Phys. Rev. Lett.* 109 (11), 114301. <https://doi.org/10.1103/PhysRevLett.109.114301>. arXiv: 1206.0461.

- Dudte, L.H., Vouga, E., Tachi, T., Mahadevan, L., 2016. Programming curvature using origami tessellations. *Nat. Mater.* London 15 (5), 583–588. <https://doi.org/10.1038/nmat4540>.
- Duncan, J.P., Duncan, J.L., 1784. *Folded developables*. *Proc. R. Soc. London Ser. A* 383 (1784), 191–205.
- Filipov, E.T., Redoutey, M., 2018. Mechanical characteristics of the bistable origami hyper. *Extreme Mech. Lett.* 25, 16–26. <https://doi.org/10.1016/j.eml.2018.10.001>.
- Filipov, E.T., Tachi, T., Paulino, G.H., 2015. Origami tubes assembled into stiff, yet reconfigurable structures and metamaterials. *Proc. Natl. Acad. Sci. U.S.A.* 112 (40), 12321–12326. <https://doi.org/10.1073/pnas.1509465112>.
- Filipov, E.T., Liu, K., Tachi, T., Schenk, M., Paulino, G.H., 2017. Bar and hinge models for scalable analysis of origami. *Int. J. Solids Struct.* 124, 26–45. <https://doi.org/10.1016/j.ijsolstr.2017.05.028>.
- Fuchs, D., Tabachnikov, S., 1999. More on Paperfolding. *Am. Math. Month.* 106 (1), 27–35. <https://doi.org/10.1080/00029890.1999.12005003>.
- Gattas, J.M., You, Z., 2014. Quasi-static impact response of alternative origami-core sandwich panels. *Am. Soc. Mech. Eng. Digital Collection*. <https://doi.org/10.1115/DETC2013-12681>.
- Gillman, A., Fuchi, K., Buskohl, P.R., 2018. Truss-based nonlinear mechanical analysis for origami structures exhibiting bifurcation and limit point instabilities. *Int. J. Solids Struct.* 147, 80–93. <https://doi.org/10.1016/j.ijsolstr.2018.05.011>.
- Giomí, L., Mahadevan, L., 2012. Multi-stability of free spontaneously curved anisotropic strips. *Proc.: Math. Phys. Eng. Sci.* 468 (2138), 511–530.
- Guest, S., Pellegrino, S., 2006. Analytical models for bistable cylindrical shells. *Proc. R. Soc. A* 462 (2067), 839–854. <https://doi.org/10.1098/rspa.2005.1598>.
- Huang, H., Hagman, A., Nygård, M., 2014. Quasi static analysis of creasing and folding for three paperboards. *Mech. Mater.* 69 (1), 11–34. <https://doi.org/10.1016/j.mechmat.2013.09.016>.
- Huffman, 1976. Curvature and creases: a primer on paper. *IEEE Trans. Comput.* C-25, 1010–1019. <https://doi.org/10.1109/TC.1976.1674542>.
- Kilian, M., Fry, S., Chen, Z., Mitra, N.J., Sheffer, A., Pottmann, H., 2008. Curved folding. In: *ACM SIGGRAPH 2008 Papers, SIGGRAPH '08*, ACM, New York, NY, USA, 2008, pp. 75:1–75:9, event-place: Los Angeles, California. <https://doi.org/10.1145/1399504.1360674>.
- Kilian, M., Monszpart, A., Mitra, N.J., 2017. String actuated curved folded surfaces. *ACM Trans. Graph.* 36 (3). <https://doi.org/10.1145/3015460>.
- Kuribayashi, K., Tsuchiya, K., You, Z., Tomus, D., Umemoto, M., Ito, T., Sasaki, M., 2006. Self-deployable origami stent grafts as a biomedical application of Ni-rich TiNi shape memory alloy foil. *Mater. Sci. Eng.: A* 419 (1), 131–137. <https://doi.org/10.1016/j.msea.2005.12.016>.
- Lang, R.J., Nelson, T.G., Magleby, S.P., Howell, L.L., 2017. Kinematics and discretization of curved-fold mechanisms, in: *Proceedings of the ASME 2017 ASME, Cleveland, OH*.
- Lechenault, F., Thiria, B., Adda-Bedia, M., 2014. Mechanical response of a creased sheet. *Phys. Rev. Lett.* 112, (24). <https://doi.org/10.1103/PhysRevLett.112.244301>.
- Lee, T.-U., You, Z., Gattas, J.M., 2018. Elastica surface generation of curved-crease origami. *Int. J. Solids Struct.* 136–137, 13–27. <https://doi.org/10.1016/j.ijsolstr.2017.11.029>.
- Liu, K., Paulino, G.H., 2017. Nonlinear mechanics of non-rigid origami: an efficient computational approach. *Proc. R. Soc. A* 473 (2206), 20170348. <https://doi.org/10.1098/rspa.2017.0348>.
- Mentrasti, L., Cannella, F., Pupilli, M., Dai, J.S., 2013. Large bending behavior of creased paperboard. I. Experimental investigations. *Int. J. Solids Struct.* 50 (20), 3089–3096. <https://doi.org/10.1016/j.ijsolstr.2013.05.018>.
- Mitani, J., Igarashi, T., 2011. Interactive design of planar curved folding by reflection. In: *Pacific Graphics, The Eurographics Association*. <https://doi.org/10.2312/PE/PG/PG2011short/077-081>.
- Miura, K., 1985. Method of packaging and deployment of large membranes in space, Tech. Rep. 618. The Institute of Space and Astronautical Science.
- Nagy, L., Rhode-Barbarigos, L., Adriaenssens, S., Kilian, A., 2015. Conceptual design of a single-crease origami-arc inspired movable footbridge Structure. *Int. J. Space Struct.* 30 (2), 75–84.
- Rodrigues, G.V., Fonseca, L.M., Savi, M.A., Paiva, A., 2017. Nonlinear dynamics of an adaptive origami-stent system. *Int. J. Mech. Sci.* 133, 303–318. <https://doi.org/10.1016/j.ijmecsci.2017.08.050>.
- Schenk, M., Guest, S.D., 2011. *Origami folding: a structural engineering approach*. In: Wang-Iverson, P., Lang, R.J., Yim, M. (Eds.), *Origami 5: Fifth International Meeting of Origami Science, Mathematics, and Education*. first ed. A K Peters/CRC Press, New York, pp. 291–303.
- Tachi, T., Epps, G., 2011. Designing one-DOF mechanisms for architecture by rationalizing curved folding.
- Tang, R., Huang, H., Tu, H., Liang, H., Liang, M., Song, Z., Xu, Y., Jiang, H., Yu, H., 2014. Origami-enabled deformable silicon solar cells. *Appl. Phys. Lett.* 104, (8). <https://doi.org/10.1063/1.4866145> 083501.
- Vergauwen, A., Laet, L.D., Temmerman, N.D., 2017. Computational modelling methods for pliable structures based on curved-line folding. *Comput. Aided Des.* 83, 51–63. <https://doi.org/10.1016/j.cad.2016.10.002>.
- Weisstein, E.W., 2019. Cone, From MathWorld – A Wolfram Web Resource. <https://mathworld.wolfram.com/Cone.html>.
- Woodruff, S.R., Filipov, E.T., 2018. Structural analysis of curved folded deployables. In: *Earth and Space 2018*. ASCE, Cleveland, OH, pp. 793–803. <https://doi.org/10.1061/9780784481899.075>.
- Woodruff, S.R., Filipov, E.T., 2020. Curved creases redistribute global bending stiffness in corrugations: theory and experimentation. *Meccanica*. <https://doi.org/10.1007/s11012-020-01200-7>.
- Yang, K., Xu, S., Shen, J., Zhou, S., Xie, Y.M., 2016. Energy absorption of thin-walled tubes with pre-folded origami patterns: numerical simulation and experimental verification. *Thin-Walled Struct.* 103, 33–44. <https://doi.org/10.1016/j.tws.2016.02.007>.
- Yasuda, H., Yein, T., Tachi, T., Miura, K., Taya, M., 2013. Folding behaviour of Tachi-Miura polyhedron bellows. *Proc. R. Soc. A* 469 (2159), 20130351. <https://doi.org/10.1098/rspa.2013.0351>.